Article:

Hu, R., Wang, J. orcid.org/0000-0003-4870-3744, Sen, B. et al. (3 more authors) (2016) PWM Ripple Currents Based Turn Fault Detection for Multiphase Permanent Magnet Machines. IEEE Transactions on Industry Applications. ISSN 0093-9994

https://doi.org/10.1109/TIA.2016.2642193

PWM Ripple Currents Based Turn Fault Detection for Multiphase Permanent Magnet Machines

Rongguang Hu, Student member, IEEE, Jiabin Wang, Senior Member, IEEE, Bhaskar Sen, Student member, IEEE, Andrew R Mills, Ellis Chong and Zhigang Sun

Abstract—Most permanent magnet machines are driven by inverters with pulse width modulation (PWM) voltages. The currents contain high frequency (HF) components which are inversely proportional to machine inductance. The HF PWM ripple currents can be used to detect a turn fault that gives rise to changes in inductance. The features of these HF components in turn fault conditions are analyzed. A bandpass (BP) filter is designed to extract the selected sideband components, and their root-mean-square (RMS) values are measured. The RMS values in all phases are compared. It is shown that the RMS ripple current ratios between two adjacent phases provide a very good means of detecting turn fault with high signal-to-noise ratio. The detection method can identify the faulted phase, tolerate inherent imbalance of the machine, and is hardly affected by transient states. The method is assessed by simulations and experiments on a five-phase permanent magnet machine.

Index Terms—Permanent magnet (PM) machines, Pulse width modulation (PWM), high frequency (HF) components, root-mean-square (RMS) measurement, turn fault detection

I. INTRODUCTION

Permanent magnet (PM) machines are becoming increasingly attractive in a variety of drive applications, due to their high performance and high efficiency. However, in these applications such as electrical vehicles (EV) [1][2] and more electric aircrafts (MEA) [3], high reliability is of great importance. An unexpected fault or failure in PM machine drives may lead to very high repair or replacement cost, or even catastrophic failure.

Turn-to-turn short circuit fault (also known as turn fault, or inter-turn fault) is one of the most severe faults [4][5]. The main cause of inter-turn faults is winding insulation deterioration as described in [6], which results from combined mechanical, electrical and thermal stresses in the stator winding. The stresses may lead to an insulation break-down of the coil conductor, which may short out some of the turns. When an inter-turn fault occurs, excessively high current will circulate in the shorted turns and increase the winding temperature to a level where severe damage or even breakdown of the whole insulation occurs [7]. In some PM machines, the large short-circuit current can produce localized magnetic field intensity higher than the coercivity of the magnets, thereby demagnetizing the magnets irreversibly [8]. Also, a large percentage of the insulation failures starts from a turn-to-turn insulation problem and subsequently develop into more severe insulation faults, such as coil-to-coil short circuit, phase-to-phase short circuit, and phase-to-ground short circuit, all of which lead to substantial damage to the machine. Therefore a swift detection of inter-turn short fault during machine operation is essential to avoid subsequent damages, and reduce repair cost and drive outage time.

In recent years, turn fault detection has been extensively studied, and various techniques and methods have been proposed. One of the most popular techniques is based on the machine current signal analysis (MCSA) [8]. The spectrum or frequency components in machine current is analyzed and recorded in healthy conditions [9][10][11][12]. Such current spectrum is different in turn fault conditions, which can be used to detect fault. From mathematical analysis, only several specific frequency components are focused since their variations are more related to fault, and can indicate fault more accurately. However, these frequency components are usually specific to a given machine. For a different machine with different rotor structure or winding configuration, the featured frequency components need to be analyzed again [13]. For most 3-phase machines, a turn-fault will cause phase unbalance and result in the amplitude difference of 3 phase current, thus generating the 2^{nd} harmonic in dq axis currents [14][15] or voltages[16]. Therefore, they have been utilized to detect the turn-fault by many researchers. In ideally balanced conditions, the 2^{nd} harmonic in dq axis currents or voltages should be zero under healthy conditions and become non-zero in fault conditions. However, due to inherent unbalance of a practical machine or other non-ideal factors in inverter and control, the 2^{nd} harmonic of dq currents or voltages is non-zero even in healthy conditions. Also, the magnitude of 2^{nd} harmonic is dependent on operating conditions. Therefore, a lookup table for the reference values in healthy conditions has to be established. While this detection technique is applicable to different types of machines, other faults, such as demagnetization or eccentricity, may also generate the same frequency component, making it difficult to distinguish these fault types[17][18].

Most of these techniques are focused on the turn fault detection in steady states. Since transient states will distort the current spectrum, traditional frequency analysis methods such as fast Fourier transform (FFT) [14], short-time Fourier transform (STFT)[19] become invalid or limited, and more advanced but more complex methods are used, such as wavelet transform (WT)[20], Hilbert-Huang transform (HHT)[21]. However, their demand for large memory and computation time usually makes it difficult to be implemented in real time.

Other researchers have used the negative sequence component of current or impedance for turn-fault detection [22]. It has been pointed out in [6] that this is equivalent to the detection technique based on the 2^{nd} harmonic. Residual current, voltage, or back electromotive force (EMF) are also utilized to detect turn fault [23][22][24], where an accurate model is used for prediction and the residual between the prediction and measurement is used for fault detection. This technique improves the signal-to-noise ratio and the effectiveness of fault detection. However, an accurate model can be difficult to obtain since some parameters, such as resistance and back-EMF, are temperature dependent. The current residual can be analyzed in each phase or in the dq reference frame as those described previously for turn fault detection [25]. Although the sensitivity and accuracy for the fault detection may be improved, the intrinsic asymmetry of the machine and drive still requires compensation. Since the machine voltages are usually not measured, the use of command voltages for predicting currents is also problematic due to inverter dead time and non-linearity.

In [4][26][27], search coils are installed in the stator teeth, and the induced voltage can be used to detect turn fault. It is said that the method is insensitive to speed and load variations, and can distinguish eccentricity, demagnetization and turn fault effectively[4], albeit they are intrusive. Unless machine is wound intentionally before implementation, there is little possibility for a general machine to be disassembled and rewound so as to employ such techniques for fault detection.

Diagnostic methods based on high frequency (HF) signal injection techniques are proposed in [28][29]. The featured HF components are actually transformed to a low frequency region, which are fundamentally the same as the negative-sequence component methods[5]. The injection of the HF signal will have a detrimental effect on drive performance and hence limit its applicability.

The detection based on PWM ripple current was first proposed in [30]. The HF currents generated by PWM voltages are utilized to detect turn fault. Thus, no extra signal injection is needed. The RMS ripple current is measured as the fault indicator, and the faulted phase can also be identified. Since the ripple current exists in healthy condition and is dependent on modulation index, or operating condition, extensive tests in order to establish a lookup map are still inevitable, and yet the map obtained in steady state tests may not be effective to monitor the machine conditions during a transient state. To circumvent these problems, this paper proposes an improved technique. A new fault indicator is defined, which is independent from operating conditions, robust to inherent unbalance, and is hardly affected by transient states. Therefore, it will be more effective for turn fault detection in all possible operating scenarios.

II. Analytical Study of HF PWM ripple currents

A. Turn fault detection technique based on PWM ripple currents

In the previous research [30], a turn fault detection technique based on PWM ripple current measurement was proposed and applied to a 10-slot, 12-pole, 5-phase surface mounted permanent magnet (SPM) machine with only one coil per phase. The geometry of the machine is shown in Fig. 1. It is an alternate tooth wound SPM machine which exhibits inherently fault tolerance due to both physical and magnetic separation of the phase windings with virtually no mutual magnetic coupling between the phases.

The schematic of a single winding of the machine under the turn fault conditions with N_f faulted turns out of a total N number turns is shown in Fig. 2. Based on the schematic, the high frequency admittance of the winding under fault conditions is derived in (1), where R_h, R_f, L_{hh} and L_{ff} are the resistance and self-inductance of the healthy and fault turns, respectively and M_{hf} is the mutual inductance between the healthy and faulted winding parts. R_f is the resistance in the shorted path and is assumed zero in the analysis for sake of simplicity. At high frequency, the difference between the admittances in turn fault and healthy conditions is more significant, making it promising for turn fault detection with high frequency signals.

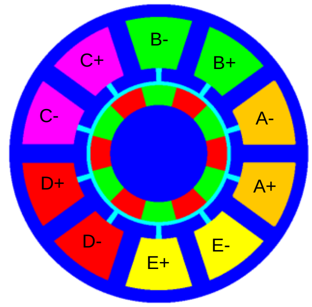

Fig. 1 Geometry of 10-slot, 12-pole SPM machine[30]

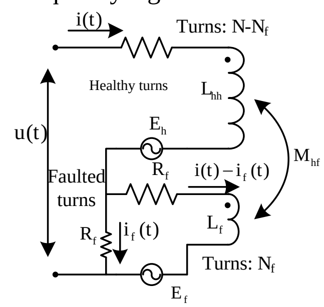

Fig. 2 Schematic of winding under turn fault[30]

$$Y(j\omega) = \frac{I(j\omega)}{V(j\omega)} = \frac{1}{R_h + j\omega L_{hh} + \dfrac{\omega^2 M_{hf}{}^2}{R_f + j\omega L_{ff}}} \tag{1}$$

The previous detection technique is based on measurement of RMS PWM ripple currents which increase in fault conditions. However, they are also dependent on operating conditions, which implies that operation-dependent thresholds have to be established by extensive tests. While such a process to determine the thresholds may be possible in a laboratory condition, it is impractical in real applications. Further the thresholds obtained in steady-state tests may not be effective for monitoring machine conditions in transient. Thus, it is desirable to develop a new fault indicator that is relatively constant in most operating conditions, and is also unaffected by transient states.

In order to determine such a fault indicator, the variation of high frequency (HF) currents due to turn fault is analyzed based on a simplified fault model. Although errors may exist in the simplified model, the results give insightful understanding of how HF currents change in fault conditions, and provide guidance to define and evaluate a new fault indicator.

B. Analysis of HF PWM ripple currents

For generality, a multi-phase machine with m number of phases is assumed. The star connection of the phase windings with their equivalent circuits and the power converter under a turn fault condition in phase A are shown in Fig. 3, where i_a, i_b,…,i_m are the phase currents, i_f is the current in the shorted branch. e_a, e_b … e_m are phase back-EMFs, L and M are self- and mutual-inductances of the healthy phases respectively. μ is the percentage of number of shorted turns N_f over the total number of turns N per phase. M_{fb}, …, M_{fm} are the mutual inductances between the faulted turns and other healthy phases, while M_{hb}, …, M_{hm} are the mutual inductances between the healthy turns and other healthy phases.

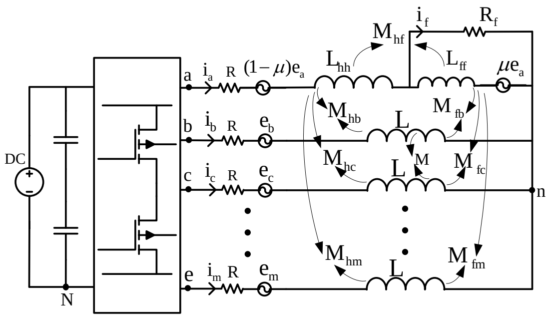

Fig. 3 Equivalent circuit under turn fault condition in phase A

Based on the equivalent circuit shown in Fig. 3, the basic equations that describe the relationships between the voltages and currents when a turn fault occurs in phase A are given in (2).

$$\begin{cases} u_{ah} = (1-\mu)Ri_a + L_{hh}\dfrac{di_a}{dt} + L_{hf}\dfrac{d(i_a - i_f)}{dt} + M_{hb}\dfrac{di_b}{dt} + \dots + M_{hm}\dfrac{di_m}{dt} + (1-\mu)e_a \\ u_{af} = \mu R(i_a - i_f) + M_{hf}\dfrac{di_a}{dt} + L_{ff}\dfrac{d(i_a - i_f)}{dt} + M_{fb}\dfrac{di_b}{dt} + \dots + M_{fm}\dfrac{di_m}{dt} + \mu e_a \\ u_a = u_{ah} + u_{af} + u_{nN} \\ u_b = Ri_b + L\dfrac{di_b}{dt} + M_{hb}\dfrac{di_a}{dt} + M_{fb}\dfrac{d(i_a - i_f)}{dt} + \dots + M\dfrac{di_m}{dt} + e_b + u_{nN} \\ \vdots \\ u_m = Ri_m + L\dfrac{di_m}{dt} + M_{hm}\dfrac{di_a}{dt} + M_{fm}\dfrac{d(i_a - i_f)}{dt} + \dots + M\dfrac{di_{m-1}}{dt} + e_m + u_{nN} \end{cases} \tag{2}$$

where u_{ah}, u_{af} are the voltages in the healthy and faulted parts of phase A winding, u_a, u_b … u_m are the inverter output voltages referred to the ground (N), u_{nN} is the voltage between the neutral point (n) and the ground. The unknown u_{nN} is obtained in (3) by summing the m voltage equations in (2) and rearranging. By eliminating it the current can be directly related to the inverter output voltage.

$$u_{nN} = \frac{\sum u_{a\dots m}}{m} + \frac{1}{m}(M_{hf} + L_{ff})\frac{di_f}{dt} + \frac{1}{m}\mu Ri_f + \frac{1}{m}(M_{fb} + \dots + M_{fm})\frac{di_f}{dt} \tag{3}$$

For high frequency currents due to PWM operation, the contribution of the back EMFs can be ignored because they are of low frequency. Hence, the equations in (2) can be rearranged by removing the back EMF and eliminating u_{nN} with (3) in the form of high frequency components in PWM voltages u_A, u_B …, u_M , shown in (4), where i_A, i_B …, i_M are high frequency currents in each phase, and i_{Fa} is the high frequency current in the shorted circuit. For the sake of simplicity, the relationship between the self- and mutual-inductances and μ may be approximated in (5), where j denotes the rest of healthy phases, b, c, …, m. This is true in the machines which have low leakage flux, or the machine with one coil per phase[31]. The basic parameters of the prototype machine in healthy and fault conditions are extracted from finite element analysis (FEA) software FLUX2D, and are shown in Table I and Table II respectively. Since this machine is a SPM machine, the saturation due to current is insignificant. Even though the short current is much larger than the rated, the effect of small number of faulted turns (2 turns in the study) on saturation is also very small. Therefore, the saturation in both healthy and fault conditions are neglected, and all the inductances are assumed to be constant.

$$\begin{aligned} & L_{hh} = (1-\mu)^2 L \\ & L_{ff} = \mu^2 L \\ & M_{hf} = \mu(1-\mu)L \\ & M_{hj} = (1-\mu)M, \quad (j = b, c, \dots, m) \\ & M_{fj} = \mu M, \quad (j = b, c, \dots, m) \end{aligned} \tag{5}$$

With (5), equations (4) can be simplified to (6), where s denotes the Laplace operator. The first m equations show the relations among the high frequency voltages, the high frequency phase currents and the fault current. It is clear that the differences in the currents are caused by the fault current, since the high frequency voltages are essentially symmetric when the frequency modulation ratio is greater than 15, and known. In healthy conditions, the fault current is zero, hence all high frequency currents should be symmetric with the same amplitude. The last equation in (6) relates the HF fault current to the HF phase A current, which can be substituted into the rest equations to establish the relation between the HF currents and HF phase voltages. After defining a coefficient k_f in (7), the final expressions for HF voltage phasors in all phases can be written in (8), in the form of corresponding HF currents and phase A voltage.

TABLE I
MACHINE DATA

Specification	Value	Specification	Value
No. of phases	5	Phase resistance	0.68
No. of poles	12	Phase inductance	2.8mH
No. of slots	10	Rated current	6.0 A
No. of turns per phase	62	Maximum speed	3000r/min
Back-EMF(peak)	37V	Rated torque	1.86 Nm
DC voltage	60V	Switching frequency	10k Hz

TABLE II
MACHINE PARAMETERS UNDER FAULT CONDITIONS

Parameter	Fault conditions	
N_f	2 turn fault	20 turn fault
R_h	0.66	0.46
R_f	0.02	0.22
L_{hh}	2.6mH	1.3mH
L_{ff}	2.8μH	0.28mH
M_{hf}	83μH	0.6mH

$$\begin{cases} u_A = (u_a - \dfrac{\sum u_{a\dots m}}{m})_{HF} = Ri_A + (L-M)\dfrac{di_A}{dt} - \dfrac{m-1}{m}(M_{hf} + L_{ff})\dfrac{di_{Fa}}{dt} - \dfrac{m-1}{m}\mu Ri_{Fa} + \dfrac{1}{m}(M_{fb} + \dots + M_{fm})\dfrac{di_{Fa}}{dt} \\ u_B = (u_b - \dfrac{\sum u_{a\dots m}}{3})_{HF} = Ri_B + (L-M)\dfrac{di_B}{dt} + \dfrac{1}{m}(M_{hf} + L_{ff})\dfrac{di_{Fa}}{dt} - M_{fb}\dfrac{di_{Fa}}{dt} + \dfrac{1}{m}\mu Ri_{Fa} + \dfrac{1}{m}(M_{fb} + \dots + M_{fm})\dfrac{di_{Fa}}{dt} \\ \vdots \\ u_M = (u_m - \dfrac{\sum u_{a\dots m}}{3})_{HF} = Ri_M + (L-M)\dfrac{di_M}{dt} + \dfrac{1}{m}(M_{hf} + L_{ff})\dfrac{di_{Fa}}{dt} - M_{fm}\dfrac{di_{Fa}}{dt} + \dfrac{1}{m}\mu Ri_{Fa} + \dfrac{1}{m}(M_{fb} + \dots + M_{fm})\dfrac{di_{Fa}}{dt} \\ 0 = \mu R(i_A - i_{Fa}) + M_{hf}\dfrac{di_A}{dt} + L_{ff}\dfrac{d(i_A - i_{Fa})}{dt} + M_{fb}\dfrac{di_B}{dt} + \dots + M_{fm}\dfrac{di_M}{dt} \end{cases} \tag{4}$$

$$\begin{cases} u_A = [(L-M)s+R]i_A - \dfrac{m-1}{m}\mu[(L-M)s+R]i_{Fa} \\ u_B = [(L-M)s+R]i_B + \dfrac{1}{m}\mu[(L-M)s+R]i_{Fa} \\ \vdots \\ u_M = [(L-M)s+R]i_M + \dfrac{1}{m}\mu[(L-M)s+R]i_{Fa} \\ i_{Fa} = \dfrac{[(L-M)s+R]}{\mu Ls+R} i_A \end{cases} \tag{6}$$

$$k_f = \frac{\mu[(L-M)s+R]}{[L+(m-1)M]\mu s+[m-\mu(m-1)]R} \tag{7}$$

$$\begin{cases} u_A = [(L-M)s+R]i_A - (m-1)k_f u_A \\ u_B = [(L-M)s+R]i_B + k_f u_A \\ \vdots \\ u_M = [(L-M)s+R]i_M + k_f u_A \end{cases} \tag{8}$$

Since the first terms in (8) are associated with the impedance in healthy conditions, the calculation and comparison of HF currents in each phase can be performed by applications of HF voltages. As the HF voltages are symmetric, it is very easy to use such a procedure to calculate the ratio of the resultant HF currents in two adjacent phases. Fig. 4 shows the schematic phasors diagram and their relative magnitudes for the 5-phase machine for a given HF voltage component.

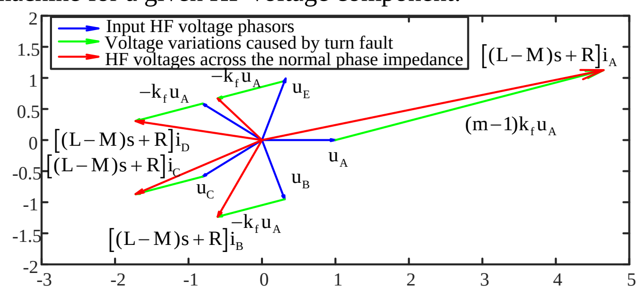

Fig. 4 Phasor plot in fault conditions

The HF voltage across the normal phase impedances should be equal to the input HF voltages in healthy conditions, but deviate from them to different extents in turn fault conditions. Since the fault occurs in phase A, the amplitude change in HF current of phase A is the largest. Although the influence of turn fault on the other phase voltage, represented by the green arrows in Fig. 4, is the same, the resultant changes of HF currents in each phase, which are proportional to the red arrows, are different.

The amplitude of HF current is dependent on HF voltages, which is determined by modulation index. Thus, a non-constant threshold whose value is related to operating conditions is needed, if turn fault detection is based on the amplitude variation of the HF currents. Since the change of the HF currents is dependent on operating conditions, the margin between the threshold and actual value to avoid false alarm is also non-constant, which compromises the sensitivity and robustness of the fault detection.

However, once a fault scenario is assumed, the phasor plot in Fig. 4 can be determined. If the HF voltages change with operating conditions, the amplitude of phasors will also change proportionally. The proportional change will not affect the relative amplitudes of the HF currents in all phases. Therefore, the comparison of HF currents in adjacent phases in the form of ratio is investigated.

III. Turn Fault Indicator Analysis

A. Prediction of HF PWM ripple currents

PWM operation of an inverter produces a specific set of high frequency voltages whose frequency and magnitude can be analyzed.

Assuming sine-PWM is employed, the frequency components of the inverter output voltage can be expressed in (9)[32], and its spectrum is shown in Fig. 5 (a).

$$\begin{aligned} v(t) &= V_D M_m \cos(\omega_r + \theta_r) \\ &+ \frac{4V_D}{\pi}\sum_{x=1}^{\infty}\frac{1}{x}J_0\left(x\frac{\pi}{2}M_m\right)\sin x\frac{\pi}{2}\cos[x(\omega_c t+\theta_c)] \\ &+ \frac{4V_D}{\pi}\sum_{x=1}^{\infty}\sum_{y=-\infty}^{\infty}\frac{1}{x}J_y\left(x\frac{\pi}{2}M_m\right)\sin\left[(x+y)\frac{\pi}{2}\right]\cos[x(\omega_c t+\theta_c)\pm y(\omega_r t+\theta_r)] \end{aligned} \tag{9}$$

where V_D is the dc voltage, M_m is modulation, ω_c is switching frequency, ω_r is the fundamental frequency, θ_r is the phase angle of the fundamental modulation signal, θ_c is the initial phase angle of the carrier wave. J_y is the Bessel function of the y^{th} order. x and y are nonnegative integers, and when x is odd, then y is even, and vice versa.

It can be seen from (9) that the frequency and magnitude of the voltage components can be expressed in (10) and in (11).

$$f = xf_c \pm yf_r \tag{10}$$

$$Ma_{xy} = \frac{4V_D}{\pi}\frac{1}{x}J_y\left(x\frac{\pi}{2}M_m\right) \tag{11}$$

where $f_c = 2\pi\omega_c$ and $f_r = 2\pi\omega_r$. The side band frequency components will only exist at xf_c, $xf_c \pm 2f_r$, $xf_c \pm 4f_r$, for x=1, 3, 5, …; and $xf_c \pm f_r$, $xf_c \pm 3f_r$, for x=2, 4, 6,…

The switching frequency of the inverter is set to 10 kHz for the machine under study, and the frequency components shown in Fig. 5 (a) accord with those in (10). After elimination of the zero sequence voltages based on (4), the spectrum of u_A is shown in Fig. 5 (b). The side band frequency components with x greater than 2 are ignored, since their amplitudes are much smaller.

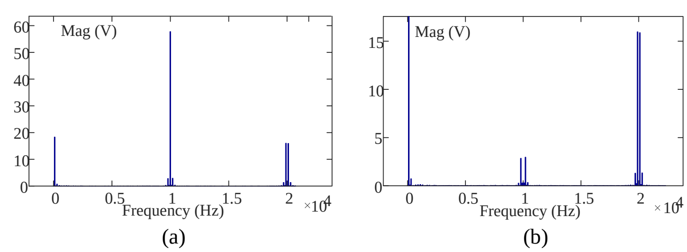

Fig. 5 (a) Spectrum of SPWM voltage. (b) Spectrum of SPWM voltage after elimination of zero sequence voltages

The magnitudes for the sideband around 10 kHz, Ma_{12}, and for the sidebands around 20 kHz, Ma_{21} and Ma_{23}, can be evaluated by (11) and their variations with modulation index are illustrated in Fig. 6. It is seen that over a wide range of modulation, the magnitude of the sideband at $2f_c \pm f_r$ is the largest. Although the magnitude at $2f_c \pm 3f_r$ is relatively small, its frequency is very close to $2f_c \pm f_r$. As a result, the combined magnitude of the two sideband HF components around 20 kHz is much larger than that around 10 kHz in most cases. These two components are chosen for further evaluation. To extract them from measured currents, a 4th order bandpass filter can be designed with the centre frequency of 20 kHz, and the band width of 2kHz.

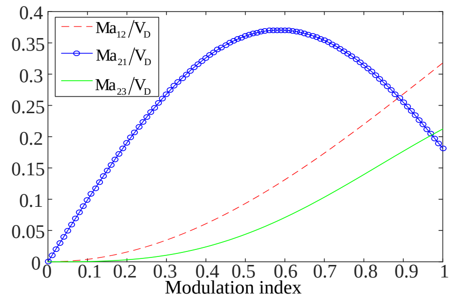

Fig. 6 Variations in sideband frequency magnitudes with modulation index

After filtering by the bandpass filter, the HF currents contain 4 frequency components, $2f_c \pm f_r$, $2f_c \pm 3f_r$. The voltage components that generate the corresponding currents are given in (12). The HF current at each frequency can be calculated by (7) and (8) as described in section II, and the admittance associated with each frequency component can be defined in (13). The expression for HF currents in phase A after filtering can be written as (14) and its root-mean-square (RMS) value is further assessed.

$$
\begin{aligned}
u_A &= u_{A3-} + u_{A-} + u_{A+} + u_{A3+} \\
&= \frac{2V_D}{\pi} \cdot \left\{ \begin{array}{l} J_3(\pi M_m)\cos[(2\omega_c - 3\omega_r)t + \theta_{u3-})] \\ -J_1(\pi M_m)\cos[(2\omega_c - \omega_r)t + \theta_{u1-})] \\ -J_1(\pi M_m)\cos[(2\omega_c + \omega_r)t + \theta_{u1+})] \\ +J_3(\pi M_m)\cos[(2\omega_c + 3\omega_r)t + \theta_{u3+})] \end{array} \right\}
\end{aligned}
\tag{12}
$$

$$
K_{a3-} = \frac{|i_{A3-}|}{|u_{A3-}|}, K_{a-} = \frac{|i_{A-}|}{|u_{A-}|}, K_{a+} = \frac{|i_{A+}|}{|u_{A+}|}, K_{a3+} = \frac{|i_{A3+}|}{|u_{A3+}|}
\tag{13}
$$

$$
i_A = \frac{2V_D}{\pi} \cdot \left\{ \begin{array}{l} K_{a3-} \cdot J_3(\pi M_m)\cos[(2\omega_c - 3\omega_r)t + \theta_{i3-})] \\ -K_{a1-} \cdot J_1(\pi M_m)\cos[(2\omega_c - \omega_r)t + \theta_{i1-})] \\ -K_{a1+} \cdot J_1(\pi M_m)\cos[(2\omega_c + \omega_r)t + \theta_{i1+})] \\ +K_{a3+} \cdot J_3(\pi M_m)\cos[(2\omega_c + 3\omega_r)t + \theta_{i3+})] \end{array} \right\}
\tag{14}
$$

B. Fault indicator

The RMS value of a signal given in (15) can be obtained by and analogue RMS converter which consists of a square function, a low-pass filter (LPF) and a root-square function, as shown in Fig. 7. Ideally, all the frequency components except the dc component should be filtered out through the low-pass filter, thus the output should be a dc signal.

$$
RMS(V_{in}) = V_{out} = \sqrt{Average(V_{in}^{\ 2})}
\tag{15}
$$

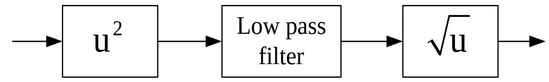

Fig. 7 Signal processing block diagram of RMS converter

When the input to the RMS converter i_A is expressed in (14), the ideal output can be written as (16). Although RMS current i_{A_rms} changes when turn fault occurs, there is no simple way to define a threshold since $i_{A\_rms\_h}$ and $i_{A\_rms\_f}$ in healthy and fault conditions are dependent on modulation index, as shown in Fig. 8. Thus, the threshold must be determined as a function of modulation index, rather than a constant, which, will increase the complexity. At low modulation index, the margin between the RMS currents in fault and healthy conditions become small, which would reduce detectability.

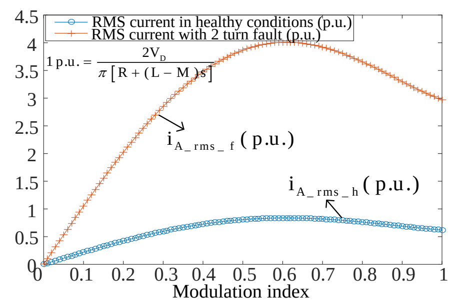

Fig. 8 Normalized RMS current variations in phase A under healthy and 2-turn fault conditions with modulation index,

Therefore, the comparison of the RMS ripple currents between phases is studied for the purpose of better fault detections. The ideal output of the RMS current for phase B can be similarly derived and is given in (17), and their ratio of the RMS currents in phases A and B under healthy and fault conditions is shown in (18). It can be shown that $K_{3a-}=K_{3b-}$, $K_{1a-}=K_{1b-}$, $K_{1a+}=K_{1a+}$, $K_{3a+}=K_{3b+}$, under healthy conditions and, hence, the ratio should be 1, regardless of modulation index. Under fault conditions, the ratio is unequal to 1, albeit it is still dependent on modulation index. The ratio variations with modulation index under healthy and 2-turn fault conditions are compared in Fig. 9 for the prototype machine whose parameters are given in Table II. It can be seen that for the whole range of modulation index from 0 to 1, the ratio in fault conditions deviates significantly from 1 and the slight variation at higher modulation index will not affect fault detection. The large deviation from the healthy value of 1 under the fault condition indicates a high signal-to-noise ratio and a constant threshold will be sufficient to ensure sensitive and robust fault detection. Further, during a transient when speed or load torque changes in healthy conditions, the modulation will change, but the ratio k_{AB_h} should remain 1 according to Fig. 9. Thus, the fault detection with the RMS current ratio as indicator will be effective in both transient and steady-state.

$$
i_{A\_rms} = \frac{2V_D}{\pi}\sqrt{[K_{3a-} \cdot J_3(\pi M_m)]^2 + [K_{1a-} \cdot J_1(\pi M_m)]^2 + [K_{1a+} \cdot J_1(\pi M_m)]^2 + [K_{3a+} \cdot J_3(\pi M_m)]^2}
\tag{16}
$$

$$
i_{B\_rms} = \frac{2V_D}{\pi}\sqrt{[K_{3b-} \cdot J_3(\pi M_m)]^2 + [K_{1b-} \cdot J_1(\pi M_m)]^2 + [K_{1b+} \cdot J_1(\pi M_m)]^2 + [K_{3b+} \cdot J_3(\pi M_m)]^2}
\tag{17}
$$

$$
k_{AB} = \frac{i_{A\_rms}}{i_{B\_rms}} = \sqrt{\frac{[K_{3a-} \cdot J_3(\pi M_m)]^2 + [K_{1a-} \cdot J_1(\pi M_m)]^2 + [K_{1a+} \cdot J_1(\pi M_m)]^2 + [K_{3a+} \cdot J_3(\pi M_m)]^2}{[K_{3b-} \cdot J_3(\pi M_m)]^2 + [K_{1b-} \cdot J_1(\pi M_m)]^2 + [K_{1b+} \cdot J_1(\pi M_m)]^2 + [K_{3b+} \cdot J_3(\pi M_m)]^2}}
\tag{18}
$$

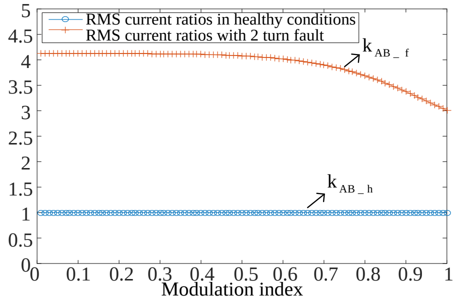

Fig. 9 Variations of RMS current ratios with modulation index under healthy and 2-turn fault conditions.

Note that the ratios for other phases can also be calculated in a similar way, but among them k_{AB} is the largest and is used as the indicator because the turn fault is assumed to occur in phase A in this case. In real applications, the faulted phase can be arbitrary, thus the ratios for each two adjacent phases need to be calculated in real time. In healthy conditions, all the ratios should be 1. In fault conditions, the ratios differ from each other. If any ratio is larger than the predefined threshold, then a fault can be detected. Also, the largest ratio can identify the phase where the turn fault occurs.

The above analysis is based on ideal conditions with simplified models for the convenience of feature extraction. The conclusion obtained is mainly qualitative, while the exact ratio under fault may not be predicted accurately. However, it can at least prove in theory that the ratios of the selected RMS ripple currents is superior to the amplitude as the turn fault indicator. The applicability of these analytic results is explored in simulation and experimental studies in the next sections.

IV. Simulation Results

The proposed turn-fault detection technique is assessed by MATLAB/SIMULINK simulations on the 5-phase fault tolerant PM machine shown in Fig. 1 with parameters listed in Table I and Table II. The 5 phases are star connected and fed by a 5-phase inverter as shown in Fig. 3. The inverter operates under sine-PWM at 10 kHz switching frequency. To accord with the analysis, a 2-turn fault is injected in phase A at 0.03s. Fig. 10 shows the phase currents in A, B, C, D and E, and their HF currents after bandpass filtering and amplifying in both healthy and 2-turn fault conditions, when the drive responds to a speed demand at 1000 r/min with i_q=6A. It is evident that the HF currents of all the phases and their RMS values are equal when the machine is healthy. When turn fault occurs in phase A, the HF and RMS currents differ among all the phases with those of phase A being the largest.

To test the robustness of fault detection in transients, the variations of speed and torque, shown in Fig. 11, are introduced in the simulation and a 2-turn fault is injected at 0.3s in phase A. The detecting results are shown in Fig. 12. In the simulation, the RMS currents are obtained by the signal processing function of the RMS converter shown in Fig. 7.

As can be observed, the RMS currents contain undesired ripples. This is because the ideal low pass filter in RMS detector is not possible and the sidebands associated with the fundamental frequency are present in the converter outputs. Thus, the output of the RMS converter will contain the frequency components at twice of the fundamental frequency which causes the output fluctuations. Consequently, the ratios also contain ripples, which makes the detection less robust if they are to be compared with a constant threshold. Thus, to eliminate these ripples, a simple low-pass filter with its corner frequency equal to the fundamental frequency can be applied to enhance the robustness of detection.

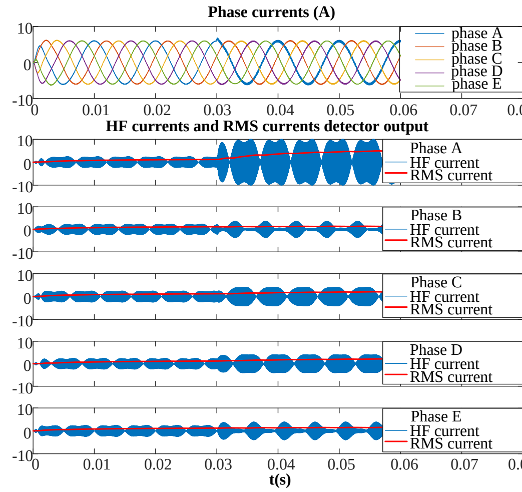

Fig. 10 HF and RMS currents in both healthy and 2-turn fault conditions

It is seen from Fig. 13 that in the healthy condition, the RMS currents in each phase are equal and the ratios are 1, and they are immune to speed variation, except for the initial transient. The step change in torque does affect the ratios slightly, but the influence is insignificant and can be ignored. The ratio deviation from 1 during the initial transient is due to the fact that there is no sufficient data for RMS calculation. After one revolution, correct RMS values in each phase are obtained, and the ratios are no longer affected by subsequent changes in speed. In the fault condition, the ratios deviate from 1 with the largest above 3. Such a large deviation gives a high signal-to-noise ratio with a constant threshold without the need for extensive experimental tests and calibrations.

If the machine has an inherent unbalance, most detection methods published in literature are affected, and data map through extensive tests is usually the only solution. The effect of phase unbalance on the proposed technique is also simulated. It should be noted that the unbalance in the back-EMFs will not have any effect on the proposed detection technique because they are of low frequency and filtered out. Hence, the simulation is performed by assuming the inductance and resistance in phase B are 3% and 5% larger than those in the other phases respectively. The simulation results are shown in Fig. 13 under the same operating conditions. As will be seen, the ratios associated with phase B under the healthy condition are slightly increased to 1.045 due to phase unbalance. However, the ratio under the fault condition is far greater. Thus, a few percent machine unbalance has little effect on this detection technique.

Fig. 14 shows the detector responses when the drive operates under the same speed and load profiles shown in Fig. 11 but the fault is injected at 0.1s during the speed transient. It is evident the detection is equally effective under the non-stationary conditions.

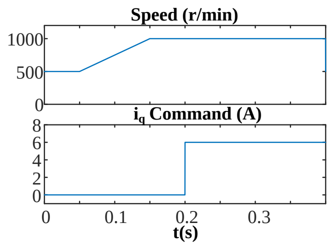

Fig. 11 Operating conditions

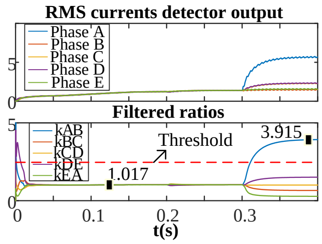

Fig. 12 RMS ripple current and fault indicator with balanced machine

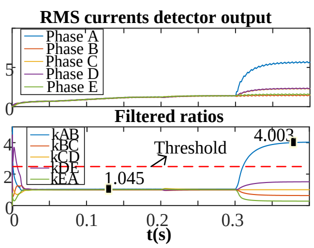

Fig. 13 RMS ripple current and fault indicator with unbalanced machine

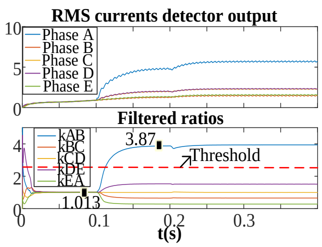

Fig. 14 Fault indicator when fault occur in non-stationary state

The robustness of the proposed method is compared with that described in [30] where the detector signal proportional to RMS ripple current is used against pre-defined thresholds as fault indicator. Fig. 15 shows the simulated fault indicators of the two methods in response to step change in load current at 500 rpm in healthy condition. If the detector signals proportional to the RMS ripple currents are to compare with the pre-defined thresholds directly, false alarms are very likely to occur as shown in the second graph of Fig. 15. This is caused by the time delay of the RMS detection. Thus, reliable detection with the technique described in [30] is only feasible in steady state. However, since the time delay for all the phases are equal, the effect on the ratio is greatly reduced. As a result, the ratio based method will not cause false alarms in transient state, enhancing the robustness and reliability of the fault detection.

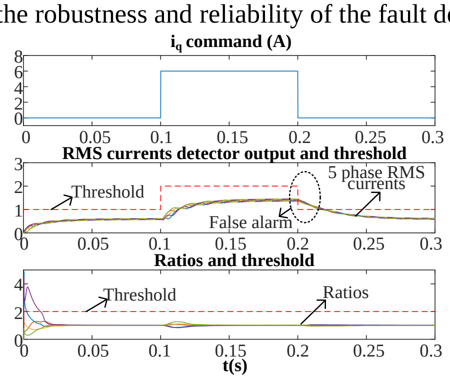

Fig. 15 Comparison of fault indicators obtained from the previous and proposed methods in transient state under healthy condition.

V. Experiment Results

The proposed turn-fault detection technique has been tested on the 5-phase prototype machine described in section Ⅱ-A. The machine is mounted on the test rig shown in Fig. 16 (a) and is controlled by the 5-phase MOSFET inverter shown in Fig. 16 (b). A 2-turn fault for short time duration is injected by the relay shown in Fig. 16 (a). The test machine operates in torque control mode with an encoder feedback and the speed is adjusted by a dynamometer. The DC link voltage is set 60V. The 5-phase fault tolerant drive system is controlled at 10 kHz switching frequency using a digital signal processor (DSP) board (EzDSP F28335). A separate analogue BP filter circuit board is designed and installed to extract the high frequency components around 20 kHz from measured phase currents and obtain their RMS values through RMS converter chips. The outputs of the RMS converters are then sampled through the ADCs (Analog to Digital Converter) of the DSP, where the ratios are calculated in real time. The diagram of the signal processing chain of the detecting technique is shown in Fig. 17.

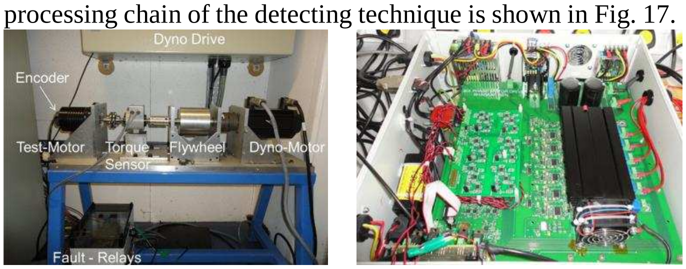

(a) (b)

Fig. 16 (a) Test rig with fault emulation set-up. (b) 5-Phase Inverter with HF detection board

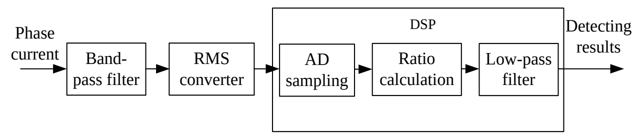

Fig. 17 Diagram of PWM ripple current based turn fault detection technique

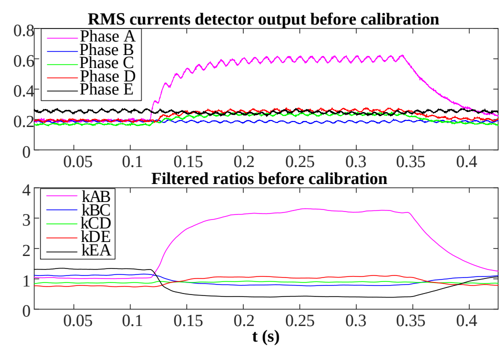

Fig. 18 Detector output with 2-turn fault in phase A before calibration, with i_q=3A and at 500 r/min.

Fig. 18 shows the detection results at i_q=3A and 500 r/min with 2-turn fault. The machine is operating in healthy conditions until 0.12s, when the 2-turn fault is injected. It can be seen that the RMS values for 5 phase HF currents are initially different in healthy conditions and the ratios are not equal to 1. This is due to a number of factors. First, a small phase unbalance is inevitable in a practical machine due to manufacturing tolerance. Second, the tolerance of capacitors used in the BP filter board is ±5% and small differences in filter gain also exist in different phases. Hence, the BP filter frequency responses in each phase are slightly different and the ratio in healthy conditions may not be 1 in an actual system. Despite of the deviation from the ideal conditions, the change of the ratios in the fault condition is still significant compared to that in healthy condition, thus the effectiveness of the ratios as fault indicator can be verified. The ripples of RMS currents are observed. To eliminate the ripples, a simple digital low-pass filter with adaptive corner frequency is applied in the DSP, and the filtered ratio is smoother and relatively constant, which will improve the robustness of the detection.

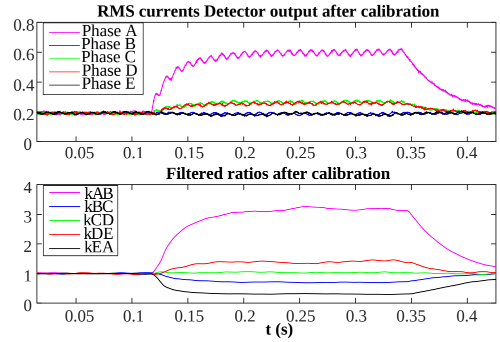

Fig. 19 Detector output with 2-turn fault in phase A after calibration, with i_q=3A and at 500 r/min.

The ratio deviation from 1 under healthy conditions can be easily corrected by a simple calibration. By way of example, the ratio, k_{AB_h}, calculated from measured RMS currents in phases A and B in healthy conditions is recorded, and a calibration coefficient is defined in (19). The coefficient is applied to obtain the calibrated ratio k_{AB}' for both healthy and fault conditions, given in (20). The calibration processes for other ratios are applied in the same manner.

$$Cali_{AB} = \frac{1}{k_{AB\_h}} \tag{19}$$

$$k_{AB}' = Cali_{AB} \cdot k_{AB} \tag{20}$$

The results after the calibration are shown in Fig. 19. The ratios are 1 in healthy conditions, while they differ significantly from 1 when the 2-turn fault occurs in phase A. The ratio, k_{AB}, under the fault condition is the largest, which can be used to identify the faulted phase. These results are consistent with the foregoing analysis and simulations. The evident change in k_{AB} provides a very effective means for detecting fault.

The sensitivity of calibration to operating conditions is further assessed. Fig. 21 and Fig. 22 show k_{AB} ratio variations before calibration with respect to speed and load current and with modulation index, respectively. It is evident that the actual ratio is not exactly but close to 1, and is virtually constant in all operating conditions. Therefore, the calibration only needs to be performed at 1 operating point. In this case, the calibration coefficient for k_{AB} is 1.08. The ratios in faulted state are also very close and distinctive from 1 for a wide range of operating conditions. Although the ratio at low speed and no load, i_q=0A, is smaller than the ratios in most operating conditions, which may be caused by machine unbalance and filter design tolerance, they have little effect on the fault detection. To compare with the technique proposed in [30], the detecting results from this technique is shown in Fig. 20. Before the detection can be effective, calibration for each phase is needed with at least 2 test operating points assuming that the RMS current is linearly proportional to modulation index. However, more data points are required if the relationship is no linear. Further, the detector outputs under the fault and healthy conditions at low speeds are so close that reliable fault detection is not possible with the method reported in [30]. However, these are not the problems in the ratio based detector as evident in Fig. 21.

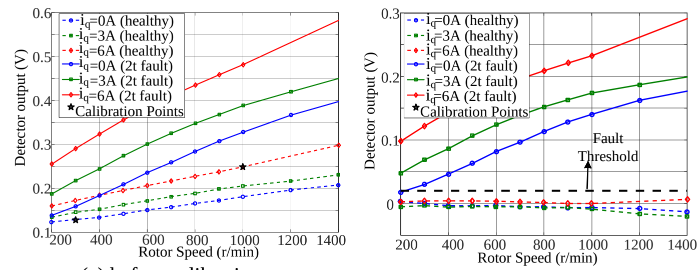

(a) before calibration (b) after calibration

Fig. 20 Variations of detector output (ph-4) with load (0%,50%,100%) and speed (a) before and (b) after calibration. [30]

In contrast, the fact that ratio of RMS current ripples in two adjacent phases is 1 in the proposed technique provides a very simple means of auto-calibration. Fig. 23 shows the ratio variations with modulation index after calibration in both healthy and fault conditions. As can been seen, a small difference in the ratio exists for a given modulation index. This is not seen from the theoretical analysis but can be explained. At the same modulation index with different combinations of i_q and speed, the effect of unbalance in phase impedance on the ripple current will be different. Further, the BP filter gains at the 4 side band frequencies are also different. These differences are ignored in the analysis, but will cause the actual ratio slightly affected by speed at a given modulation index. However, these differences are insignificant, and will not affect the detection. The experimental results verify the significant differences in the fault indicator in healthy and fault conditions, which implies that the proposed technique has a high signal-to-noise ratio, which enhances the robustness of the turn fault detection.

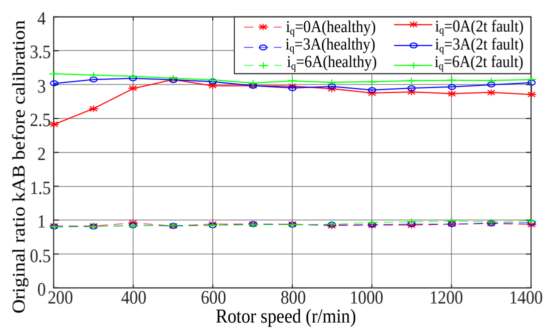

Fig. 21 Variations of ratio k_{AB} with load current and speed before calibration

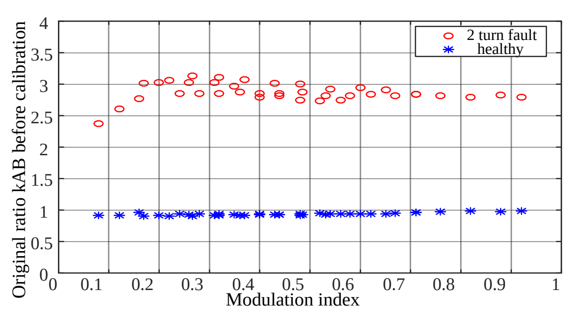

Fig. 22 Variations of ratio k_{AB} with modulation index before calibration

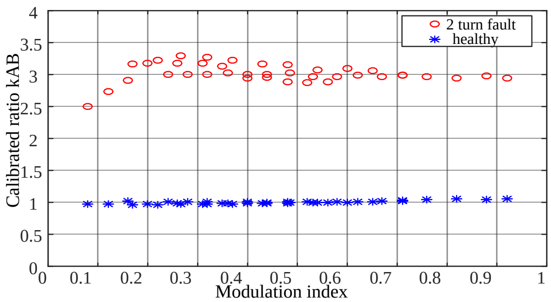

Fig. 23 Variations of calibrated ratio k_{AB} with modulation index under healthy and fault conditions

Fig. 24 shows the detector output during transient in healthy condition. At 500 r/min, a step change in load current from 0A to 3A is applied to i_q at 0.2s. A slight speed variation is witnessed from the waveform of phase current i_A due to limited disturbance rejection capacity of the dynamometer. Despite this, the ratio processed by the DSP is hardly affected. A similar test is performed with the machine operating at 500 r/min and i_q=1A, and the 2-turn fault is initiated at 0.2s and removed at 0.42s. The resultant phase current, fault current and fault indicator are shown in Fig. 25. The fault current increases from 0A to 10A, and the ratio changes immediately from 1 to 3 when the fault occurs. The effect of LPF to remove the ripple in the original ratio can also be seen. Although it will introduce additional delay, the effect is not significant as the fault can be detected within 0.05s with the threshold set at 2.

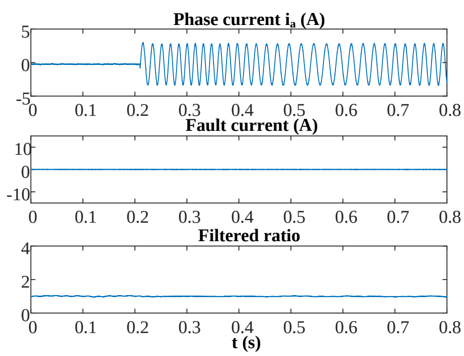

Fig. 24 Current waveforms and detector output with load step change of i_q from 0A to 3A at 0.2s in healthy conditions at 500 r/min

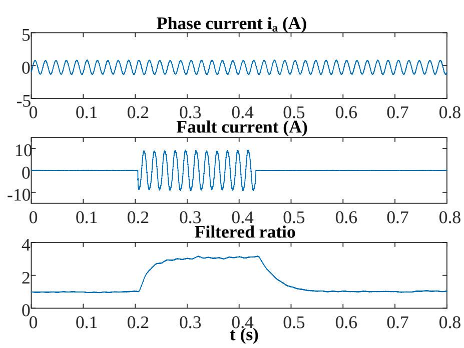

Fig. 25 Current waveforms and detector output with 2-turn fault at 0.2s at i_q=1A, 500 r/min

While the developed technique is verified on the 5-phase SPM machine which exhibits negligible effect of magnetic saturation, it should also be applicable to machines whose parameters are significantly affected by magnetic saturation, such as interior permanent magnet (IPM) machines. This is because under healthy conditions, the multi-phase machine is balanced and the ratios of PWM current ripples between two adjacent phases should be 1.0 regardless of operating (or saturation) conditions. If a turn fault occurs in one of its phases, the incremental inductance at a given operating condition in each phase becomes different and hence the ratios would deviate from 1.0, which provides an effective means of detecting the fault. The details of the application of the proposed detection technique to IPM machines will be reported in future.

VI. Conclusion

The proposed turn fault detecting technique utilizes the HF currents generated by PWM voltages directly without the need of extra HF signal injection. The RMS values of the selected HF PWM currents are obtained by analogue BP filters and RMS converters which are required as extra electronic circuits, and the ratios between the RMS currents from two adjacent phases are calculated and employed as the fault indicator. It has been shown that the non-ideal factors, such as phase unbalance and tolerances in the filter components can be effectively removed by a simple calibration. Thus, the implementation of the proposed technique is convenient without the need of a lookup table. The simulation and experiments also show that the proposed technique is effective in both transient and steady states.

References

[1] Z. Q. Zhu and D. Howe, "Electrical Machines and Drives for Electric, Hybrid, and Fuel Cell Vehicles," Proc. IEEE, vol. 95, no. 4, pp. 746–765, 2007.

[2] K. T. Chau, C. C. Chan, and C. Liu, "Overview of permanent-magnet brushless drives for electric and hybrid electric vehicles," IEEE Trans. Ind. Electron., vol. 55, no. 6, pp. 2246–2257, 2008.

[3] W. Cao, B. C. Mecrow, G. J. Atkinson, J. W. Bennett, and D. J. Atkinson, "Overview of electric motor technologies used for more electric aircraft (MEA)," IEEE Trans. Ind. Electron., vol. 59, no. 9, pp. 3523–3531, 2012.

[4] Y. Da, X. Shi, and M. Krishnamurthy, "A new approach to fault diagnostics for permanent magnet synchronous machines using electromagnetic signature analysis," IEEE Trans. Power Electron., vol. 28, no. 8, pp. 4104–4112, 2013.

[5] P. Zhang, Y. Du, T. G. Habetler, and B. Lu, "A survey of condition monitoring and protection methods for medium-voltage induction motors," IEEE Trans. Ind. Appl., vol. 47, no. 1, pp. 34–46, 2011.

[6] S. Grubic, J. M. Aller, B. Lu, and T. G. Habetler, "A survey on testing and monitoring methods for stator insulation systems of low-voltage induction machines focusing on turn insulation problems," IEEE Trans. Ind. Electron., vol. 55, no. 12, pp. 4127–4136, 2008.

[7] R. Z. Haddad and E. G. Strangas, "Fault detection and classification in permanent magnet synchronous machines using Fast Fourier Transform and Linear Discriminant Analysis," 2013 9th IEEE Int. Symp. Diagnostics Electr. Mach. Power Electron. Drives, pp. 99–104, 2013.

[8] A. Gandhi, T. Corrigan, and L. Parsa, "Recent advances in modeling and online detection of stator interturn faults in electrical motors," IEEE Trans. Ind. Electron., vol. 58, no. 5, pp. 1564–1575, 2011.

[9] B. M. Ebrahimi, J. Faiz, and S. Member, "Feature Extraction for Short-Circuit Fault Detection in Permanent-Magnet Synchronous Motors Using Stator-Current Monitoring," IEEE Trans. Power Electron., vol. 25, no. 10, pp. 2673–2682, 2010.

[10] J. C. Urresty, J. R. Riba, and L. Romeral, "Diagnosis of interturn faults in pmsms operating under nonstationary conditions by applying order tracking filtering," IEEE Trans. Power Electron., vol. 28, no. 1, pp. 507–515, 2013.

[11] L. Romeral, J. C. Urresty, J. R. Riba Ruiz, and A. Garcia Espinosa, "Modeling of surface-mounted permanent magnet synchronous motors with stator winding interturn faults," IEEE Trans. Ind.

Electron., vol. 58, no. 5, pp. 1576–1585, 2011.

[12] G. M. Joksimovic and J. Penman, "The detection of inter-turn short circuits in the stator windings of operating motors," IEEE Trans. Ind. Electron., vol. 47, no. 5, pp. 1078–1084, 2000.

[13] H. Saavedra, J. C. Urresty, J. R. Riba, and L. Romeral, "Detection of interturn faults in PMSMs with different winding configurations," Energy Convers. Manag., vol. 79, pp. 534–542, 2014.

[14] K. H. Kim, "Simple online fault detecting scheme for short-circuited turn in a PMSM through current harmonic monitoring," IEEE Trans. Ind. Electron., vol. 58, no. 6, pp. 2565–2568, 2011.

[15] K.-H. Kim, D.-U. Choi, B.-G. Gu, and I.-S. Jung, "Online fault-detecting scheme of an inverter-fed permanent magnet synchronous motor under stator winding shorted turn and inverter switch open," IET Electr. Power Appl., vol. 4, no. 4, p. 214, 2010.

[16] T. Boileau, N. Leboeuf, B. Nahid-Mobarakeh, and F. Meibody-Tabar, "Stator winding inter-turn fault detection using control voltages demodulation," 2012 IEEE Transp. Electrif. Conf. Expo, ITEC 2012, vol. 1, 2012.

[17] B. M. Ebrahimi, J. Faiz, and M. J. Roshtkhari, "Static-, dynamic-, and mixed-eccentricity fault diagnoses in permanent-magnet synchronous motors," IEEE Trans. Ind. Electron., vol. 56, no. 11, pp. 4727–4739, 2009.

[18] J. Cusido, L. Romeral, J. a. Ortega, J. a. Rosero, and A. Garcia Espinosa, "Fault Detection in Induction Machines Using Power Spectral Density in Wavelet Decomposition," IEEE Trans. Ind. Electron., vol. 55, no. 2, pp. 633–643, 2008.

[19] W. G. Zanardelli, E. G. Strangas, and S. Aviyente, "Identification of Intermittent Electrical and Mechanical Faults in Permanent Magnet AC Drives Based on Time-Frequency Analysis," IEEE Trans. Ind. Appl., vol. 43, no. 4, pp. 1–10, 2007.

[20] M. Khan and M. a. Rahman, "Development and Implementation of a Novel Fault Diagnostic and Protection Technique for IPM Motor Drives," IEEE Trans. Ind. Electron., vol. 56, no. 1, pp. 85–92, 2009.

[21] C. Wang, X. Liu, and Z. Chen, "Incipient stator insulation fault detection of permanent magnet synchronous wind generators based on hilbert-huang transformation," IEEE Trans. Magn., vol. 50, no. 11, 2014.

[22] R. M. Tallam, T. G. Habetler, and R. G. Harley, "Stator winding turn-fault detection for closed-loop induction motor drives," IEEE Trans. Ind. Appl., vol. 39, no. 3, pp. 720–724, 2003.

[23] N. Leboeuf, T. Boileau, B. Nahid-Mobarakeh, G. Clerc, and F. Meibody-Tabar, "Real-time detection of interturn faults in PM drives using back-EMF estimation and residual analysis," IEEE Trans. Ind. Appl., vol. 47, no. 6, pp. 2402–2412, 2011.

[24] A. Sarikhani, S. Member, and O. A. Mohammed, "Inter-Turn Fault Detection in PM Synchronous Machines by Physics-Based Back Electromotive Force Estimation," IEEE Trans. Ind. Electron., vol. 60, no. 8, pp. 3472–3484, 2013.

[25] Y. Mollet, X. Kestelyn, F. Meinguet, E. Semail, and J. Gyselinck, "Change-detection algorithm for short-circuit fault detection in closed-loop AC drives," IET Electr. Power Appl., vol. 8, no. 5, pp. 165–177, 2014.

[26] K. T. Kim, S. T. Lee, and J. Hur, "Diagnosis technique using a detection coil in BLDC motors with interturn faults," IEEE Trans. Magn., vol. 50, no. 2, pp. 2–5, 2014.

[27] Z. Sun, J. Wang, D. Howe, and G. W. Jewell, "An online winding fault detection technique for fault-tolerant PM machines," Int. J. Syst. Sci., vol. 40, no. 3, pp. 289–296, 2009.

[28] F. Briz, M. W. Degner, A. Zamarron, and J. M. Guerrero, "On-line stator winding fault diagnosis in inverter-fed ac machines using high frequency signal injection," Ind. Appl. Conf. 2002. 37th IAS Annu. Meet. Conf. Rec., vol. 3, no. 4, pp. 2094–2101, 2002.

[29] F. Briz, M. W. Degner, P. García, and A. B. Diez, "High-frequency carrier-signal voltage selection for stator winding fault diagnosis in inverter-fed AC machines," IEEE Trans. Ind. Electron., vol. 55, no. 12, pp. 4181–4190, 2008.

[30] B. Sen and J. Wang, "Stator Inter-Turn Fault Detection in Permanent Magnet Machines Using PWM Ripple Current Measurement," IEEE Trans. Ind. Electron., vol. 0046, no. c, pp. 1–1, 2016.

[31] B. Vaseghi, B. Nahid-Mobarakh, N. Takorabet, and F. Meibody-Tabar, "Inductance identification and study of PM motor with winding turn short circuit fault," IEEE Trans. Magn., vol. 47, no. 5, pp. 978–981, 2011.

[32] T. Lipo and D. G. Holmes, "Pulse Width Modulation for Power Converters," no. Wiley-IEEE Press, 2003.

Rongguang Hu (S'16) was born in China. He received B.Eng. degree and M.Sc. degree in electrical engineering from Nanjing University of Aeronautics and Astronautics, Nanjing, China, in 2012 and 2015, respectively.

He is currently pursuing the Ph.D. degree in electronic and electrical engineering at The University of Sheffield, U.K. His current research interests include power-electronic control of electric machines, sensorless control and fault diagnosis.

Jiabin Wang (SM'03) received the B.Eng. and M.Eng. degrees from Jiangsu University of Science and Technology, Zhenjiang, China, in 1982 and 1986, respectively, and the Ph.D. degree from the University of East London, London, U.K., in 1996, all in electrical and electronic engineering.

Currently, he is a Professor in Electrical Engineering at the University of Sheffield, Sheffield, U.K. He was a Postdoctoral Research Associate at the University of Sheffield, Sheffield, U.K., from 1996 to 1997, and a Senior Lecturer at the University of East London from 1998 to 2001. His research interests range from motion control and electromechanical energy conversion to electric drives for applications in automotive, renewable energy, household appliances and aerospace sectors.

He is a fellow of the IET and a senior member of IEEE.

Bhaskar Sen (S'11) received the B.E. degree from Delhi College of Engineering, Delhi, India in 2003, M.Tech. degree from Indian Institute of Technology, Kanpur, India in 2006 and Ph.D. degree from the University of Sheffield, UK in 2015. From 2006 to 2011, he worked as a research engineer with GE Global Research, Bangalore, India. Currently he is working as a research associate in the University of Sheffield, UK. His current research interests include electrical machine fault modelling, machine fault detection.

Andrew R Mills, CEng, PhD, is a Senior Researcher and Research Programme Manager at the University of Sheffield. He has worked in the defence industry on aerospace and automotive applications before his current post within the University Technology Centre supported by Rolls-Royce. Research interests are in the application of control systems engineering principles to a broad range of applied control and health management research challenges.

Ellis Chong, PhD, CEng, MIET, received his PhD degree in electrical engineering from the University of Cambridge in 2001. He is a chartered electrical engineer and has been working in the transport and power industries in the areas of electrical machines and power electronics since 2001. He is currently the Electrical Machines and Power Electronics Team Leader in the Electrical Capability Group in Rolls-Royce Plc.

Zhigang Sun received his PhD degree in Electrical Engineering from the University of Sheffield in 2009. He has been working in the field of electrical power systems in various professional roles in aerospace industry, semiconductor industry and higher education since 2009. He is currently an Electrical Engineer at Electrical Capability Group at Rolls-Royce plc.